Photoemission Study of the Thermoelectric Group IV-VI van der Waals Crystals (GeS, SnS, and SnSe)

Agata K. Tołłoczko, Szymon J. Zelewski, Jakub Ziembicki, Natalia Olszowska, Marcin Rosmus, Tomasz Woźniak, Sefaattin Tongay, and Robert Kudrawiec*

Group IV-VI van der Waals crystals (MX, where M = Ge, Sn, and X = S, Se) are receiving increasing attention as semiconducting thermoelectric materials with nontoxic, earth-abundant composition. Among them, SnSe is considered the most promising as it exhibits a remarkably high thermoelectric figure of merit (*ZT*), initially attributed to its low lattice thermal conductivity. However, it has been shown that the electronic band structure plays an equally important role in thermoelectric performance. A certain band shape, described as a "pudding mold" and characteristic for all MXs, has been predicted to significantly improve *ZT* by combining good electrical conductivity with high Seebeck coefficient. This subtle feature is explored experimentally for GeS, SnS, and SnSe by means of angle-resolved photoemission spectroscopy. The technique also allows for the determination of the effective mass and Fermi level position of as-grown undoped crystals. The findings are supported by ab initio calculations of the electronic band structure. The results greatly contribute to the general understanding of the valence band dispersion of MXs and reinforce their potential as high-performance thermoelectric materials, additionally giving prospects for designing systems consisting of van der Waals heterostructures.

1. Introduction

A family of van der Waals crystals isoelectronic to black phosphorus called group IV monochalcogenides (MXs)[1] are known to be promising for application in two-dimensional (2D) optoelectronics (light detectors, solar cells)[2–7] and piezotronics.[8–10] Recently, they have also been rediscovered as potentially excellent thermoelectric materials,[11–13] extremely desired in the era of growing energy demand, as they possess the ability to convert waste heat into electricity. A quantity dictating the efficiency of thermoelectric conversion is a dimensionless thermoelectric figure of merit $ZT = \frac{S^2 \sigma T}{\kappa_L + \kappa_e}$, where S is the Seebeck coefficient (or thermopower), σ is the electrical conductivity, κ_L and κ_e are, respectively, lattice and electronic thermal conductivities, and T is the temperature. Materials with high ZT values (>2.0) are desired for efficient thermoelectric devices, unfortunately the parameters involved in the equation are interdependent, thus improving one often leads to deterioration of the other. Two strategies are commonly exploited to obtain high ZT: minimizing the thermal conductivity, and maximizing the power factor $PF = S^2\sigma$. The former is commonly realized by nanostructuring, dimensionality reduction, and introducing heavy atoms, which reduce the lattice thermal conductivity.[14–16] The latter can be achieved by electronic band structure engineering and adjustment of the Fermi level position by changing the charge carrier concentration.[17–21] Fermi level pinned deep inside the semiconductor band gap and high density of states at the band top (in the case of materials with simple band structure, dominated by a single valley, ensured by large effective mass) are favorable for large Seebeck coefficient, but result in poor electrical conductivity. However, it has been found that more complex band dispersion, with multiple valleys in the proximity of chemical potential, may allow to combine these two properties, by providing sufficient density of states and simultaneously preserving low effective mass.[22,23] What is more, Kuroki and Arita[24] discovered that these conditions can be fulfilled by a single electronic band of a certain shape, described as "pudding mold", characterized by effectively flat band top and strongly dispersive sidebands. Both features (multivalley transport and "pudding mold" shape) can be found in the band structure of group IV monochalcogenides. The representatives of MXs attracting increasing attention are GeS, GeSe, SnS, and SnSe – layered semiconductors composed of earth-abundant and nontoxic elements, crystalizing in orthorhombic *Pnma* structure. Out of the four,

A. K. Tołłoczko, S. J. Zelewski, J. Ziembicki, T. Woźniak, R. Kudrawiec
Department of Semiconductor Materials Engineering
Wrocław University of Science and Technology
Wybrzeże Wyspiańskiego 27, Wrocław 50-370, Poland
E-mail: agata.tolloczko@pwr.edu.pl

N. Olszowska, M. Rosmus
Solaris National Synchrotron Radiation Centre
Jagiellonian University
Czerwone Maki 98, Kraków 30-392, Poland

S. Tongay
School for Engineering of Matter, Transport and Energy
Arizona State University
Tempe, AZ 85287, USA

The ORCID identification number(s) for the author(s) of this article can be found under https://doi.org/10.1002/adom.202302049

DOI: 10.1002/adom.202302049

SnSe has been the most thoroughly studied[17,18,25–31] since Zhao et al.[32] reported a remarkably high ZT of 2.63 at 923 K. Considering the state-of-the-art nanostructured PbTe-based thermoelectric materials with $ZT = 2.2$,[14] such result was unexpected for a simple as-grown crystal composed of relatively light atoms. The authors attribute this property to ultralow intrinsic lattice thermal conductivity, resulting from strong lattice anharmonicity,[33,34] although later complementary explanations have been proposed, involving the electronic band structure.[17,27] Soon characteristic multivalley and pudding-mold band dispersion predicted by Density Functional Theory (DFT) calculations has been confirmed by angle resolved photoemission spectroscopy (ARPES).[17,27,29,30] Good thermoelectric performance has also been theoretically predicted for other MXs,[11,12] but significantly less attention was paid compared to SnSe. The second most popular is SnS, for which ZT exceeding 1 was achieved and the electronic band structure was experimentally investigated.[19,35–38] GeSe follows tin chalcogenides with several reports of ARPES[39,40] and thermoelectric properties measurements,[41,42] while for GeS only computational simulations have been published to date.[43–46] Therefore, especially for this material an experimental investigation is required to provide insight into its most fundamental properties and verify the calculations. Generally, according to both theoretical predictions and empirical studies, compared to SnSe other MXs exhibit poorer thermoelectric performance, which however does not necessarily exclude them from applications in thermoelectric devices. It has been shown that high ZT values can be obtained for heterostructures,[47,48] and, what is more, the increased efficiency of Peltier cooling can be reached by introducing a gradient of Seebeck coefficient across the device.[49]

In this work we present an in-depth investigation of the electronic band structure of GeS, SnS, and SnSe by combined ARPES measurements and DFT calculations. ARPES is the only technique allowing to experimentally observe the valence band dispersion, and additionally determine other important properties of the material, such as Fermi level position and hole effective mass. The obtained results are discussed in terms of thermoelectric performance of MXs and other potential applications. For SnS and SnSe previous findings are confirmed and augmented with investigations at higher binding energies. For GeS a first-to-date comprehensive experimental study of the valence band dispersion allowing to observe the "pudding mold" band shape is presented.

2. Results and Discussion

2.1. Crystal Structure and Simulated Electronic Band Dispersion

In **Figure 1**a–c schematic diagrams of MX crystal structure are presented. MXs crystalize in orthorhombic phase belonging to space group *Pnma* (no. 62), with two characteristic orthogonal crystallographic directions, armchair (x) and zigzag (y). A single layer is composed of two rows of atoms bound covalently, as can be seen in the side view of a layer in Figure 1b,c. The armchair direction is characterized by a peculiar puckered atomic arrangement, absent in the zigzag direction, which leads to strong in-plane anisotropy of these materials.[34,50–57] In a multilayer structure the layers are sequenced in a centrosymmetric AB stacking (particular atoms are positioned differently in alternating layers), but again only in the armchair direction (see Figure 1b). In a monolayer (or few, odd-number layer flakes) the inversion symmetry is broken, resulting in piezoelectric,[8–10] multiferroic,[58–60] and nonlinear optical properties.[61–64]

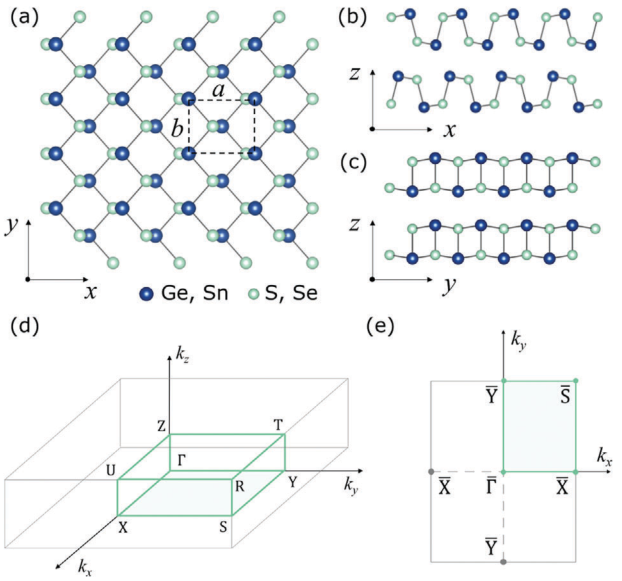

Figure 1. Schematic diagrams of crystal structure of the MXs, visualizing the atomic arrangement in a) a layer plane, and b) along the armchair, and c) the zigzag directions. d) 3D and e) reduced 2D Brillouin zone of the orthorhombic lattice, with marked high-symmetry points.

An investigation of the electronic band dispersion, either experimentally or theoretically, demands an understanding of the reciprocal lattice of MXs. In Figure 1d the first Brillouin zone (BZ) of a simple orthorhombic structure is presented, with marked high symmetry points. Such picture represents the three-dimensional (3D) BZ, characteristic for bulk crystals. Directions parallel to k_x and k_y wavevector components correspond to the in-plane armchair and zigzag directions of the real space, respectively, and k_z corresponds to the direction perpendicular to the layer plane. However, in ARPES technique the results are usually analyzed with regard to the 2D (surface) BZ, presented in Figure 1e. In this case four characteristic high-symmetry points ($\bar{\Gamma}$, $\bar{Y}$, $\bar{X}$, and $\bar{S}$) are the projections along k_z of the respective points of the 3D BZ. Further, we also introduce the Λ and Δ symbols in order to label characteristic points in the Γ-X (close to X point) and Γ-Y (approximately in half of the distance between Γ and Y) paths, respectively, where the valence band local maxima occur. Analogously, their projections onto the 2D reduced BZ are referred to as $\bar{\Lambda}$ and $\bar{\Delta}$.

The electronic band structure along the high symmetry paths of the 3D BZ obtained from DFT calculations with the use of HSE06 hybrid functional for each investigated material is illustrated in **Figure 2**. Both valence and conduction band dispersions are plotted, allowing to determine the type and theoretical width of the electronic energy gap. The computation procedure (see the Experimental Section for details) did not involve the determination of the Fermi level position, therefore the energy scale is relative to the energy of the highest valence band maximum (VBM) of each structure. As can be seen from Figure 2, a common feature

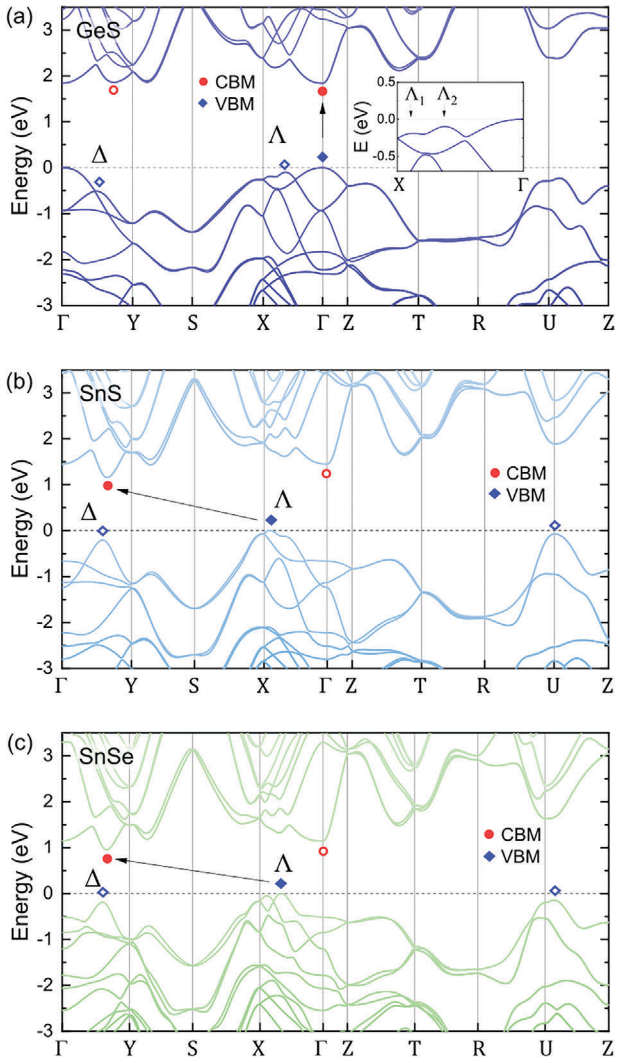

Figure 2. Electronic band structure predicted by DFT calculations with the HSE06 hybrid functional for a) GeS, b) SnS, and c) SnSe. The red circles and blue diamond symbols mark conduction band minima and valence band maxima, respectively. Solid symbols correspond to main extrema of the structure. The inset of panel (a) illustrates the separation of the band apices in the Λ region. The energy of the highest VBM is assumed as E = 0 eV.

of all MXs is the presence of multiple band extrema within a narrow energy range, marked with red circles (conduction band minimum, CBM) and blue diamond symbols (VBM). Solid symbols correspond to the lowest CBM and highest VBM, determining the band gap, whereas hollow ones denote secondary extrema. For tin chalcogenides, the main VBM is located in the Γ-X path close to the X point, in a k-region labeled Λ. The topmost band forms a characteristic pudding mold shape,[17,24] with two closely lying maxima separated by a shallow minimum (a saddle point). In the case of GeS, an analogous feature is also present, although the valley at the Γ point plays the role of the highest VBM. To better resolve the pudding mold structure, a close-up of the Λ region is presented in the inset of Figure 2a for GeS. The exact k-points where the maxima occur are referred to as Λ_1 (closer to the X point) and Λ_2 (farther from the X point). The same nomenclature is used for SnS and SnSe. The predicted band shape diverges from an ideal pudding mold, as the band tops in Λ_1 and Λ_2 are located at slightly different energies, as demonstrated in Figure S1 (Supporting Information). Another important feature is the secondary VBM located in approximately half of the Γ-Y path, in a point labeled Δ, at the energy of ≈100 meV below the Λ maximum for SnS and SnSe, and ≈500 meV for GeS. A high energy valley is also present in (or close to) the U point, which is located above the X point in the k_z direction of the BZ. It is worth noticing that the splitting into the Λ_1 and Λ_2 apices vanishes away from the central plane of the BZ to form a single broad maximum in the U point. The energies of the discussed features are summarized in Table S2 (Supporting Information).

The conduction band dispersion of the MXs is similarly complex. For GeS the lowest CBM is located at Γ, suggesting a direct character of the band gap, although there are two other valleys, in the Γ-Y and Y-S paths, at nearly the same energy (≈10 and ≈30 meV higher, respectively). With such small differences, it is not possible to unambiguously determine the band gap character of GeS based solely on the DFT simulations, although regarding the proximity of multiple valleys, either in the valence and conduction band, a direct-like behavior can be expected to manifest in the material properties. The domination of the optical properties by direct optical transitions, despite the indirect fundamental band gap, has been shown for another group IV monochalcogenide – GeSe.[52,65] In the case of SnS and SnSe the CBM appears near the Δ point, however at not the same k-value as the VBM_Δ. According to these observations, tin chalcogenides have an indirect energy gap. The theoretical values of the band gaps can be found in Table 2.

The simulations discussed above were performed with the use of the HSE06 hybrid functional, which is established as a method allowing to accurately reproduce the band dispersion. Nevertheless, DFT calculations are always burdened with approximations and the final result may vary depending on the choice of the computational method and parameters. According to our overall experience with the MX family, it is the lattice optimization procedure that affect the resulting band dispersions most severely. In our previous work regarding GeS, the structure optimization was performed applying the same procedure (see Experimental Section), but with different parameters and van der Waals correction.[54] The resulting band structure varied from the one presented here, with the most significant discrepancies being the positions of the highest VBM (in the Λ region instead of Γ point) and lowest CBM (in the Γ-Y path instead of Γ point), and, as a consequence, indirect instead of direct band gap character. In this work, for an optimized crystal structure, we compare two methods of the electronic dispersion calculation: the commonly used HSE06 hybrid functional, and modified Becke-Johnson exchange potential (mBJ-TB09), which characterizes with significantly lower computational cost. A comparison of the electronic band structures calculated for GeS, SnS, and SnSe acquired with the two methods is presented in Figure S2 (Supporting Information). The differences in the dispersion near the valence band top are minor, and become more distinct at deeper energy levels, where the bands obtained from HSE06 calculations are visibly shifted toward higher binding energies with respect to mBJ. Most importantly, the relative energies of the

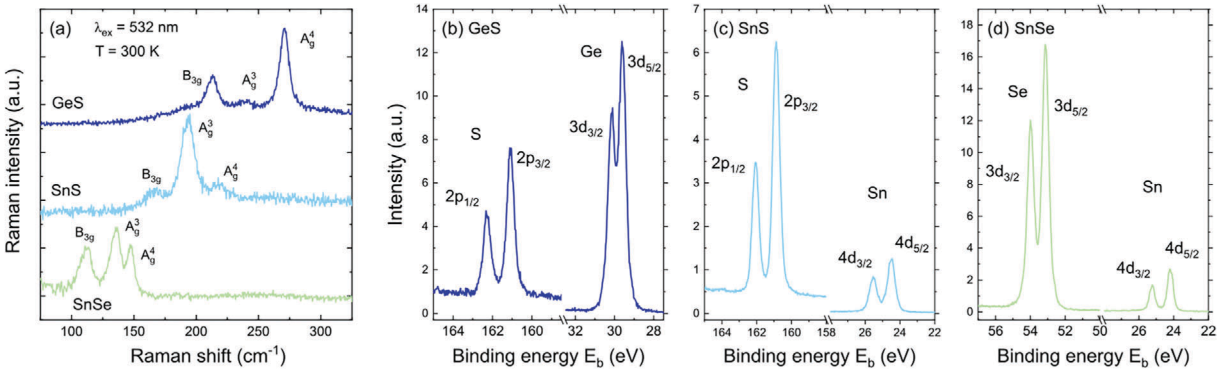

Figure 3. a) Raman scattering spectra with identified vibrational modes, and core level XPS lines observed for b) GeS, c) SnS, and d) SnSe.

band extrema are preserved. Eventually, mBJ calculations result in slightly narrower band gaps, however the differences are less than 60 meV. Therefore, it can be concluded that for the purpose of the band dispersion reproduction in proximity of the band gap, both methods provide similar results, with the mBJ-TB09 being considerably less resource- and time-consuming.

An electronic structure with multiple band extrema leads to some major consequences, that need to be discussed. First of all, a multivalley structure may significantly improve the thermoelectric properties of a material (effectively increased density of states leads to the enhancement of the Seebeck coefficient).[22,23,26] Bands in close vicinity of the Fermi level can contribute to the electronic transport through thermal excitation or increasing the carrier concentration by doping. Importantly, the pudding mold shape of a band is considered a feature responsible for combining good conductivity with large thermopower. In Figure S1a (Supporting Information) a simplified pudding mold structure is schematically presented. When the separation between the maxima and the central minimum is within the order of magnitude of thermal energy $k_B T$, where k_B is the Boltzmann constant, and T is the temperature, a significant part of the band is effectively flat, resulting in high-effective-mass-like conditions, favorable for large thermopower. Meanwhile, strongly dispersive sidebands (correlated with low effective mass) ensure good conductivity. The influence of the pudding mold band shape on thermoelectric properties of the material is discussed in detail by Kuroki and Arita.[24]

According to previous reports, the valence band of the MXs is composed of a mixture of chalcogen atom p orbitals (S 3p or Se 4p) and group-IV atom s orbitals (Ge 4s or Sn 5s). The conduction band is dominated by the Ge 4p or Sn 5p states, with minor contribution from S or Se.[53,54]

In the following sections, the calculated band dispersion is discussed with regard to the experimentally observed valence band structure, acquired with the use of ARPES technique.

2.2. Structural Characterization

The measured samples were bulk undoped crystals, grown by chemical vapor transport (CVT) method. The quality and purity of the crystals were confirmed by Raman scattering and x-ray photoemission spectroscopy (XPS). Raman scattering measurements (**Figure 3**a) revealed only vibrational modes characteristic for the considered crystallographic system (symmetric A_g and asymmetric B_{3g} shear vibrations[66,67]), with no evidence of chalcogen-rich phase, indicating high structural quality of the examined crystals. An investigation of the qualitative chemical composition was performed using core level XPS (Figure 3b–d). The full-scale spectra, plotted in Figure S3 (Supporting Information), only show the presence of Ge or Sn and S or Se atoms in the measured binding energy range. Investigations of oxygen-related levels, laying outside the range for which the beamline equipment is optimized, are not considered relevant due to the process of sample preparation, involving exfoliation under ultra-high vacuum ($<10^{-9}$ mbar), allowing to minimize surface oxidation. In Figure 2b–e regions of the spectra with characteristic features related to particular elements are presented, for GeS (panel b), SnS (c), and SnSe (d). For S in GeS and SnS a doublet corresponding to 2p orbitals was observed, with spin-orbit (SO) splitting of 1.16 eV, and expected $p_{3/2} : p_{1/2}$ intensity ratio of ≈2:1. For Se in SnSe, a 3d doublet can be identified, with SO splitting of 0.86 eV, and the $d_{5/2} : d_{3/2}$ intensity ratio of ≈3:2. For Ge (Sn) atoms, signal associated with 3d (4d) orbitals was detected, with SO splitting of 0.54 eV (1.04 eV). Additionally, for GeS a weak contribution from Ge 3p orbitals was measured (see inset of Figure S3a, Supporting Information). The obtained values of binding energy indicate either +2 or −2 oxidation state of metal and chalcogen atoms, respectively, and no sidebands originating from other phases (MX_2, M_2X_3), oxides, or elemental forms were observed.[68,69] Raman modes and XPS core level lines observed in the experiments, with corresponding frequencies, binding energies, and SO splitting values, are summarized in the Supporting Information (Table S1).

2.3. Photoemission Study

An experimental investigation of the electronic band structure performed by means of ARPES measurements is a straightforward way to observe the actual valence band dispersion and verify the accuracy of the theoretical model used for its prediction indicating the directions for future improvements. It allows to directly connect certain features occurring in the band structure with the resulting properties of the material, such as thermoelectric performance, band gap character, and optical transitions (including their anisotropy), without the influence of approximations and corrections.

For the interpretation and discussion of ARPES results we assume a 2D BZ, presented in Figure 1e. The choice of the k_x-k_y plane containing the center of the BZ, i.e., the Γ point, is justified in this case. While for covalent 3D materials the electronic bands dispersion in the k_z direction is usually significant, most vdW crystals characterize with quasi-2D structure, which leads to weak dispersion in the direction corresponding to the layers stacking axis. Nevertheless, the considered surface BZ is a projection of the bulk BZ, therefore a contribution of other states along k_z may still be visible in the photoemission maps. In the experiment, different values of k_z can be probed by adjusting the incident photons energy. Such test scans within the energy range from 40 to 100 eV were performed and no apparent dispersion was in fact observed, which is consistent with reports of Pletikosić et al. regarding SnSe.[27] Follow-up experiments were carried out at a constant photon energy of 100 eV, allowing to acquire a picture of a large region of the reciprocal space.

In **Figure 4** the results of ARPES measurements are summarized and set with DFT calculations of the electronic band structure, obtained using the HSE06 hybrid functional. Panels a, b, and c demonstrate maps acquired for GeS, SnS, and SnSe, respectively. For clarity, each panel has been divided into subpanels indexed from 1 to 6. In this section the energy corresponding to the highest VBM (E_{VBM}) for each sample is assumed as relative zero ($E_{VBM} = 0$), and all results are presented with respect to this energy. The Fermi level position and actual binding energies of the VBMs are discussed later.

An important mode of the ARPES technique is the investigation of constant energy contours in the k_x-k_y plane. Subpanels (1) and (2) for each material present maps of photoemission intensity as a function of the in-plane wavevector. White dashed rectangles represent the boundaries of the first BZ, with high symmetry points labeled in Figure 4a$_2$. In subpanels (1) maps corresponding to the energy close to the highest VBM of each material are shown, and in subpanels (2) features below VBM are visualized. In Figure 4a$_2$ a constant energy contour corresponding to 3.0 eV below the VBM of GeS reveals four equivalent valleys in $\bar{S}$ points, revealing the rectangular shape of the BZ and allowing to directly determine its dimensions. For SnS and SnSe a similar structure appears at slightly different energies, as presented in Figure S4 (Supporting Information). Figure 4b$_2$ and c$_2$ show maps at energies of -0.40 eV and -0.36 eV, respectively, where secondary VBMs of tin chalcogenides become distinct. Another approach in the analysis of ARPES results, allowing more in-depth investigation of the electronic structure, its anisotropy, and direct interpretation in terms of DFT calculations, is to map photoemission along selected high-symmetry directions in wide binding energy range. Such scans can be compared side-by-side with band structure predicted by DFT. Subpanels (3) and (5) show ARPES maps along $\bar{X}$-$\bar{\Gamma}$-$\bar{X}$ and $\bar{Y}$-$\bar{\Gamma}$-$\bar{Y}$ paths of the 2D BZ. In subpanels (4) and (6) calculated valence band dispersion is superimposed over the second derivative of the photoemission map.

As can be seen from the figures, each investigated material exhibits anisotropy of the band dispersion, with the pudding mold shape of the topmost band in the $\bar{\Lambda}$ region (labeled in Figure 4c$_1$). Although the characteristic splitting into Λ_1 and Λ_2 valleys is challenging to detect experimentally, thanks to high angular resolution of the utilized setup we were able to observe it. This feature was clearly visible for SnSe (see Figure 4c), and less conspicuous for GeS and SnS. Close-ups of the photoemission maps and their second derivatives containing the $\bar{\Lambda}$ region are presented in Figure S5 (Supporting Information). The measured dispersion does not exactly follow the calculated one, which may be attributed to the influence of other k_z states. DFT predicts different energies of the maxima in Λ_1 and Λ_2 points, separated by up to 70 meV, while in the case of GeS and SnSe the shape observed in the photoemission maps is more symmetrical. Both maxima occur at approximately equal energy, and the central minimum is significantly shallower, which makes each hole pocket accessible simultaneously. Such a shape is also closer to an ideal pudding mold. For SnS the agreement with calculations is better – the VBM in Λ_2 is located below Λ_1, which may partly account for poorer thermoelectric performance compared to SnSe.

In the case of GeS, there is a crucial discrepancy between experiment and theory regarding the position of the main VBM. According to calculations, the highest VBM occurs at the Γ point, and the Λ valleys lay ≈100 meV below, whereas in the ARPES maps in Figure 4a$_1$,a$_3$ it is clearly visible, that all three maxima correspond to nearly equal binding energy. Assuming the lowest CBM in the Γ point, GeS turns out to be a direct or a quasi-direct semiconductor, which is consistent with previously reported optical spectroscopy investigations,[50,70,71] however in order to definitely determine the band gap character, also the conduction band dispersion needs to be investigated experimentally.

For SnS and SnSe there are distinct differences between calculated and measured band dispersion around the Γ point, especially in the k_x direction. In the calculated structure the bands are extremely flat and form a saddle point (with positive curvature in the k_x direction, and negative in the k_y). In the experiment, an isotropic parabolic maximum was observed, with stronger dispersion. The bands energy, however, still remains significantly below the VBM_Λ, and therefore their contribution to optoelectronic properties of the material is minor.

The secondary VBM in the Δ point is clearly visible for tin chalcogenides, and its position can be most accurately determined from constant energy contours, corresponding to an energy at which the band emerges (see Figure S4, Supporting Information). For SnSe the VBM_Δ is located at −0.22 eV, and for SnS at −0.26 eV, however the photoemission originating from this BZ region is weak, preventing us from a more precise estimation of the energy. The results for both compounds are in agreement with our DFT HSE06 calculations (predicting the energies of −0.19 and −0.20 eV, respectively), as well as with previous experimental studies on SnSe (reporting a distance from the VBM_Λ of 0.20–0.26 eV[26–28]). For GeS this feature could not be resolved in the ARPES measurements due to high-intensity band around Γ, overlapping photoemission originating from the Δ valley, although the observed band shape follows the simulated dispersion (see Figure 4a$_6$).

In general, considering a wide binding energy range, the valence band dispersion obtained from ARPES measurements is in outstanding agreement with DFT predictions, and the observed discrepancies can be explained and justified. To begin with, the ARPES maps are projections of the 3D band structure onto a 2D plane, while the DFT calculations discussed here only simulate the dispersion along high symmetry paths in the bulk BZ.

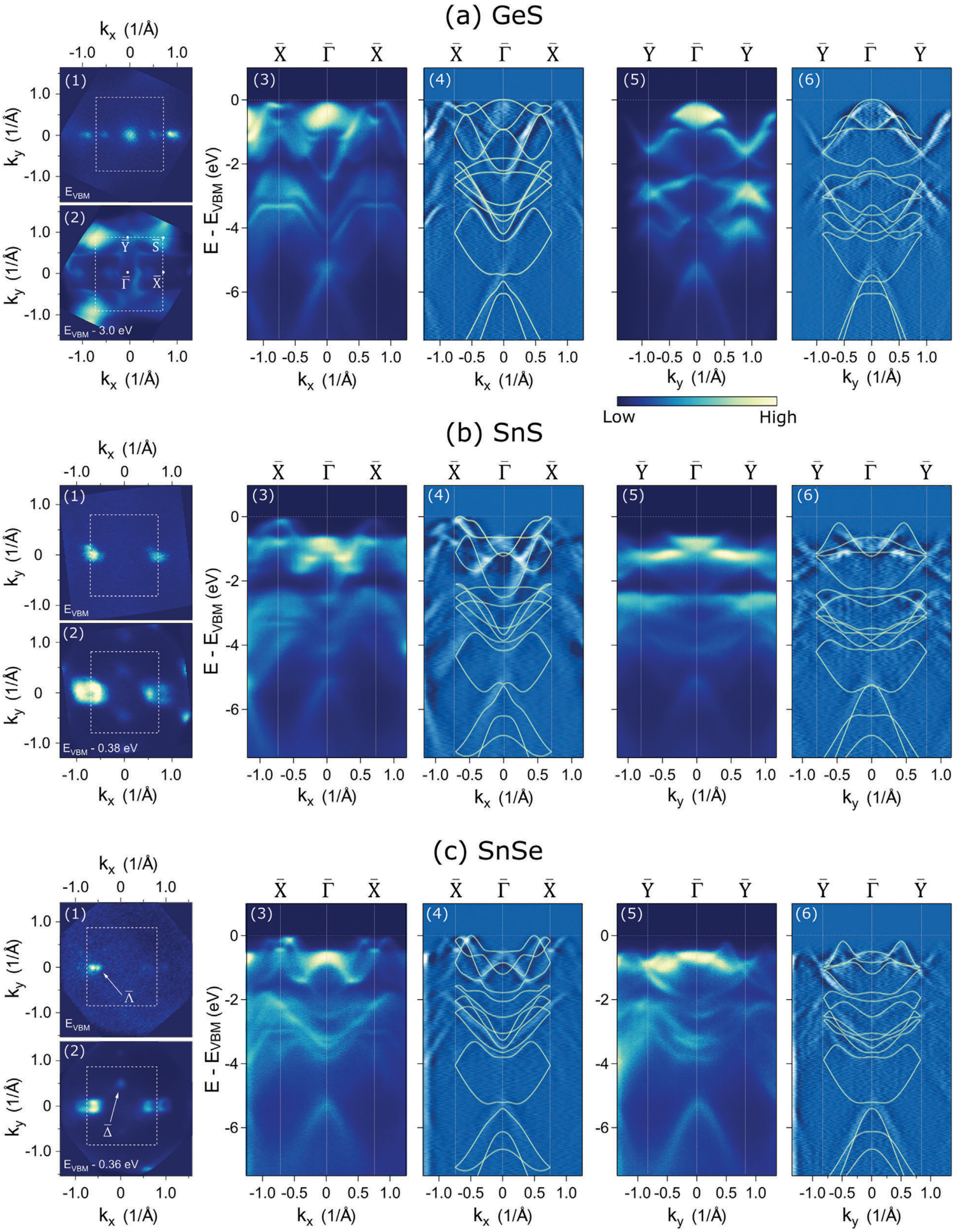

Figure 4. The results of ARPES measurements of valence band dispersion for a) GeS, b) SnS, and c) SnSe. Subpanels (1) and (2) present constant energy contours acquired at the band tops and energies at which other important features occur. White dashed rectangles mark the boundaries of the first BZ. In subpanels (3) and (5) photoemission maps in kx and ky directions, respectively, are shown, and in subpanels (4) and (6) valence band structure calculated with the HSE06 hybrid functional is superimposed over second derivative of the corresponding photoemission maps.

The measurement resolution is also limited by the experimental setup and configuration (temperature, width of the detector slits, incident photon energy, etc.), which does not apply to theoretical predictions. On the other hand, the DFT calculation results strongly depend on the choice of computational method and vdW correction, as discussed in Section 2.1, and to some degree do not accurately reproduce the actual electronic band structure. At last, the experimentally observed intensity of particular bands depends on the photoemission matrix element, which may result in weak or even invisible bands. There is, though, an interesting feature common for all investigated crystals present in the ARPES spectra, but not in the calculated band structure, which is unusual. In the X point of the BZ a narrow band emerges at the energy of ≈3 eV below the VBM, which exhibits remarkably flat dispersion in the k_x direction in quite wide wavevector range, implying strong localization. One explanation for such a picture might be a superposition of multiple bands with weak dispersion, resulting in one effectively flat band, although in such case we would expect larger broadening. The contribution from other k_z states should be considered, however no comparably flat bands at the corresponding energies were predicted in the U point of the 3D BZ either. This feature could be also interpreted as a measurement artifact (a ghost band resulting from step-like character of the sample surface), yet it is highly unlikely, as it appears for each sample. The most probable explanation is to attribute this band to some kind of an intrinsic defect level, common for the whole MX family, which explains both the flat dispersion (strong localization) and the lack of corresponding feature in the calculated band structure (assuming perfect crystal lattice). Nevertheless, to determine and understand the true origin of the discussed band, further investigation is required.

2.4. Effective Mass

The effective mass m^* of a material is determined by the curvature of the electronic band and given by $m^* = \frac{\hbar^2}{2}\left(\frac{\partial E^2}{\partial^2 k}\right)^{-1}$, where E is the energy, and k is the wavevector. Assuming parabolic approximation around the band top, m^* can be evaluated by fitting the dispersion with quadratic function. Such approach can be exploited for both theoretically and experimentally obtained band structure, however in the case of ARPES maps multiple factors may affect the result. The estimated band curvature strongly depends on the choice of the points indicating the band edge, which is often to some extent arbitrary, considering the image resolution and steepness of the observed feature. For this reason, significant discrepancies can be found in the literature. Most works regarding the hole effective mass focus on the SnSe compound.[26–29,38,72,73] The reported values of m_h^* in the Λ region of the BZ in the k_x direction range from 0.12 m_0[26] to 0.24 m_0,[73] and in the k_y direction from 0.1 m_0[38] up to 0.38 m_0[29] (where m_0 is the free electron mass). Also the ratio of the effective mass components in k_x and k_y directions varies, in some works reported as greater than 1, in others below 1.

Here we were able to evaluate the hole effective mass for SnS and SnSe around VBMs in the Λ_1 and Λ_2 points separately. In the case of GeS the photoemission originating from this BZ region was too weak to precisely determine m_h^*, and only estimations were made, burdened with high uncertainties. As the secondary VBM, the Γ point was analyzed for GeS, and the Δ point for SnS and SnSe. The m_h^* values were obtained by fitting of the parabolic function to the band edges visible in the photoemission second derivative maps, as presented in **Figure 5**. For each material (Figure 5b–d) the index of the subpanel (1-5) corresponds to a particular cut through the BZ, as labeled in Figure 5a. The determined values are summarized in **Table 1**. For SnSe we obtained good agreement with previously reported results. Besides a slightly higher effective mass at the Λ valley in the k_x direction, the values coincide perfectly with those reported by Pletikosić et al.[27] ($m_x^{\Lambda} = 0.21\ m_0$, $m_y^{\Lambda} = 0.18\ m_0$, $m_y^{\Delta} = 0.24\ m_0$), which we consider the most reliable due to quality and resolution of the acquired ARPES maps. The experimental effective masses are generally in accordance with theoretical values, listed in Table S3 (Supporting Information), obtained by fitting the parabolic function to calculated band dispersion around VBMs. The values closest to the experiment were found for SnSe (in Λ_1, Λ_2, and Δ points) and GeS (in the Γ point). The most significant discrepancies occurred for the Λ_1 point in the case of GeS, and the Λ_2 point in the case of SnS.

The effective mass is a parameter directly influencing the carrier mobility ($\mu = \frac{e\tau_c}{m^*}$, where e is the elementary charge, and τ_c is the mean free time between collisions), and, as a consequence, the electrical conductivity of a given type ($\sigma = en\mu$, where n is the carrier concentration). Therefore, the ratio of the values corresponding to respective crystallographic directions can be compared. In the Δ region the m_x/m_y ratio is generally greater than 1 for tin chalcogenides and below 1 for GeS. The exact values are listed in Table 1. This result is in agreement with reports of hole mobility and conductivity measured in armchair and zigzag directions. According to Tian et al.,[36] for SnS the hole mobility ratio $\mu_y/\mu_x = 1.67$. For SnSe Zhao et al.[32] report $\mu_y/\mu_x = 2$, but along with the electrical conductivity ratio of $\sigma_y/\sigma_x = 1.2$. Such comparison may not be entirely accurate due to the influence of τ_c parameter, which along with the effective mass often exhibits anisotropy and is affected by the presence of defects. Nevertheless, we can see that the general tendency is preserved: for tin chalcogenides the conductivity is better in the zigzag direction, while for GeS the armchair direction is preferable (like in the case of black phosphorus[74]).

2.5. Fermi Level Position

In the previous sections we assumed the energy corresponding to the highest VBM as the relative zero level, in order to conveniently compare the acquired photoemission maps with DFT predictions. However, for the design of electronic devices and heterostructures the position of Fermi level needs to be investigated. In ARPES measurements the Fermi level energy (E_F) can be determined by using a reference gold sample. Accordingly, the VBM position (E_{VBM}) with respect to the E_F was found for GeS, SnS, and SnSe corresponding to the energies of 0.67, 0.38, and 0.14 eV, respectively. The value obtained for GeS is larger than reported by Smiles et al. (0.46 eV),[69] however their experiment was carried out at room temperature, not 77 K, as in the case of this work, and the shift of the E_F toward the valence band may be a consequence of thermal activation of intrinsic acceptors. For SnS and SnSe our results are in line

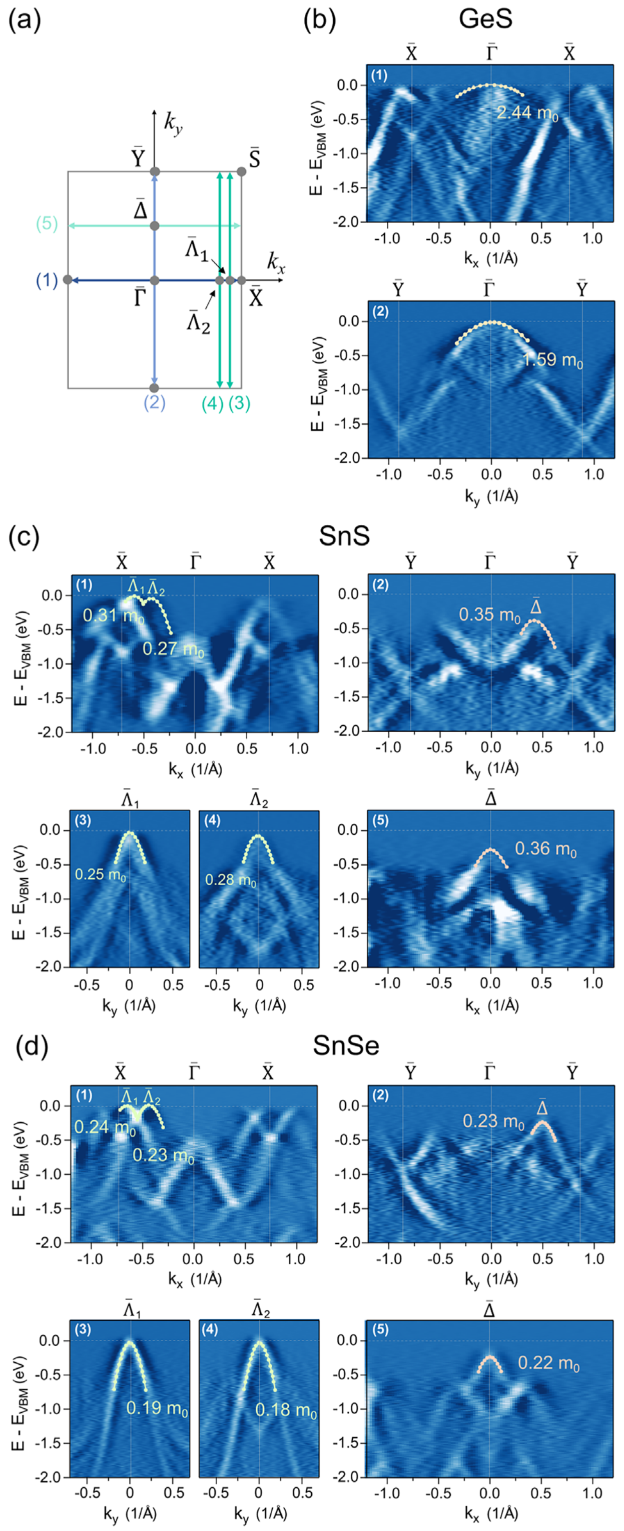

Figure 5. a) 2D Brillouin zone of MXs with marked cuts, along which the effective mass was investigated. Photoemission second derivative maps of the VBMs in the Λ region and the Γ or the Δ point of the BZ acquired for b) GeS, c) SnS, and d) SnSe, with results of fitting the parabolic function to dispersion at the band tops, in order to extract the hole effective mass. The subpanels (1)–(5) correspond to the respective cuts given in panel (a).

Table 1. Hole effective masses of GeS, SnS, and SnSe in the Λ_1, Λ_2, and Γ or Δ points of the BZ, along k_x and k_y directions, determined from ARPES maps. The values are given as fractions of the free electron mass m_0.

BZ point	Λ_1			Λ_2			Γ or Δ		
	m_x	m_y	m_x/m_y	m_x	m_y	m_x/m_y	m_x	m_y	m_x/m_y
GeS	≈0.3	≈0.7	≈0.43	–	–	–	2.44 (Γ)	1.59 (Γ)	1.53
SnS	0.31	0.25	1.24	0.27	0.28	0.96	0.28 (Δ)	0.35 (Δ)	0.80
SnSe	0.24	0.19	1.26	0.23	0.18	1.28	0.22 (Δ)	0.23 (Δ)	0.96

with Whittles et al. (≈0.38 eV for SnS)[68] and Pletikosić et al. (0.12 eV for SnSe).[27]

In order to assess the CBM position (E_{CBM}) relative to E_F, the energy gap (E_g) of each material is necessary. E_g can be determined from DFT calculations of the electronic band structure, although such approach i) provides the value at temperature of 0 K, and ii) may vary dependently on the choice of the computational method. Therefore, we performed experimental investigation by means of the optical absorption spectroscopy, at the temperature of ≈80 K. From the Tauc plots[75] of the acquired spectra (presented in Figure S6, Supporting Information) we obtained the band gaps of 1.69 eV for GeS, 1.15 eV for SnS, and 0.98 eV for SnSe. In the case of GeS the direct character of the band gap was assumed (for the reasons explained before), contrary to tin chalcogenides. Considering these results, the Fermi level position indicates p-type character for all materials, which is in accordance with previous reports.[68,69,76] The determined values of E_{VBM}, E_{CBM}, and E_g are summarized in **Table 2**, and in **Figure 6** the band alignment with respect to the Fermi level of the investigated samples is presented. Based on the obtained results an important observation can be made, that GeS forms type I heterojunction with either SnS or SnSe. On the other hand, a composition of the two tin chalcogenides results in a type II structure. In terms of thermoelectric efficiency, the position of E_F closer to the band top is favorable for maximizing the PF. Additionally, by comparing the experimental band gaps with theoretical ones, it can be decided which computational method provides a more accurate value. As it turns out, for GeS both procedures result in similar energies and overestimate the band gap by more than 100 meV. For tin chalcogenides the agreement with the experiment is generally better, and the HSE06 hybrid functional allows to obtain more accurate values.

Table 2. Valence and conduction band energies with respect to the Fermi level of GeS, SnS, and SnSe, together with band gaps determined from optical absorption measurements. All experiments were performed at the temperature of ≈80 K. Theoretical band gaps (E_g^{theor}) were obtained from DFT calculations (performed with either HSE06 or mBJ-TB09 procedure) and correspond to the temperature of 0 K.

	E_{VBM} [eV]	E_{CBM} [eV]	E_g^{exp} [eV]	E_g^{theor} [eV]	
				HSE06	*mBJ-TB09*
GeS	−0.67	1.02	1.69	1.84	1.83
SnS	−0.38	0.77	1.15	1.16	1.10
SnSe	−0.12	0.84	0.98	0.95	0.89

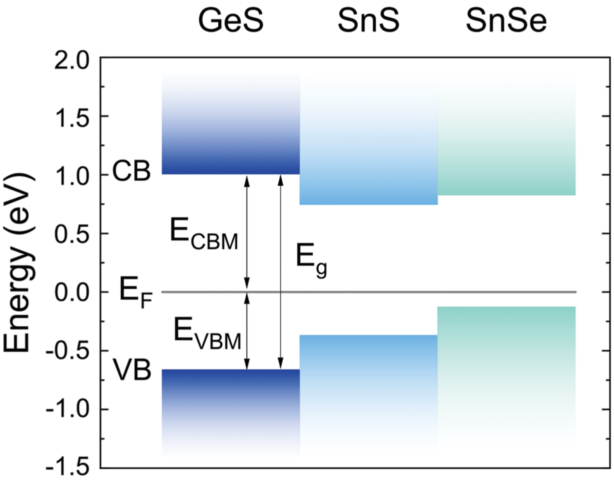

Figure 6. A band diagram of a hypothetical GeS/SnS/SnSe heterostructure with conduction and valence band alignment with respect to the Fermi level, determined for the investigated materials.

3. Conclusion

In conclusion, we performed a series of experiments exploiting the ARPES technique on orthorhombic group IV monochalcogenides GeS, SnS, and SnSe, along with complementary DFT calculations of the electronic band structure. The obtained results were analyzed in terms of the influence of the valence band dispersion on the thermoelectric performance and other properties of the materials. In the acquired high-resolution photoemission maps we were able to observe multiple valleys in the proximity of chemical potential and characteristic pudding mold shape of the band near the X point of the Brillouin zone, with two hole pockets separated by a shallow minimum. These two features are responsible for combining high Seebeck coefficient with good conductivity and play an important role in increasing the thermoelectric figure of merit (ZT).[22,24,26] From the obtained results hole effective masses and Fermi level positions of each sample were determined. Additionally, band gaps were found using optical absorption measurements. SnSe turned out to exhibit the lowest effective mass of ≈0.20 m_0, VBM energy closest to Fermi level, at −0.14 eV, and narrowest band gap of 0.98 eV at 80 K. These findings are in line with reports of the superior electrical conductivity of SnSe, and along with low lattice thermal conductivities contribute to remarkably high ZT of 2.62.[32] Due to wider band gaps and Fermi levels farther from the VBM, intrinsic GeS and SnS exhibit poorer conductive properties, these features are however favorable for high Seebeck coefficient. The obtained experimental results are generally in accordance with DFT predictions, although a few discrepancies were noticed, reinforcing the importance of the experimental investigation. In the case of GeS, most importantly, a step toward the band gap character determination was made by experimental observation of two valence band apices (in the Γ and Λ points) at equal binding energies (not predicted by the simulations). Although for a complete picture of the band structure the conduction band dispersion needs to be yet examined, our results, combined with previous optical measurements, are in favor of direct or quasi-direct energy gap, crucial for multiple applications.

A direction worth exploring is also the investigation of MX-based heterostructures and alloys, as it has been found that certain combinations of the materials can result in either type I or type II heterojunction, and introducing a gradient of ZT across a thermoelectric device (Peltier cooler) may in some conditions improve its performance.[49]

4. Experimental Section

The investigated samples were nominally undoped GeS, SnS, and SnSe single crystals, grown by iodine-assisted chemical vapor transport technique in vacuum-sealed quartz ampoules (15 cm in length, 2.4 cm outer diameter, 2.0 cm inner diameter). The growth temperature and pressure were 900–1100 °C and $\approx 10^{-5}$ mbar, respectively. To initiate nucleation and facilitate the transport of the precursors a temperature difference of ≈50 °C between hot and cold zones of the ampule was created.

Preparation of the samples for photoemission experiments (ARPES, XPS) involved mechanical exfoliation in ultra-high vacuum conditions ($<10^{-9}$ mbar), at room temperature. For Raman and optical absorption spectroscopies flakes of a thickness of 50–100 nm were selected. No special treatment was needed.

Raman scattering measurements were conducted exploiting a custom optical setup, consisting of a 550 mm focal length grating monochromator coupled with a liquid nitrogen cooled CCD array detector camera. For sample excitation a 532 nm laser diode was used, with incident power of 250 µW and laser spot size of ≈5 µm, focused by a 50×, NA = 0.55 magnifying objective lens, also allowing signal collection in the backscattering mode. The experiment was carried in ambient conditions.

The photoemission studies (ARPES, XPS) were performed using synchrotron radiation at the URANOS beamline of the SOLARIS National Synchrotron Radiation Centre (Kraków, Poland),[77] The photoemission signal was detected with Scienta-Omicron DA30-L electron analyzer. The measurements were performed at the temperature of 77 K (achieved in a flow-type liquid nitrogen cryostat) and base pressure below 5×10^{-11} mbar. Along with GeS, SnS, and SnSe, an attempt to perform complementary measurements for the fourth member of the MX family, GeSe, was made. Unfortunately, the sample suffered degradation under the illumination with high-energy photons, making it impossible to acquire satisfactory results.

Optical absorption spectra, allowing to determine the energy gap of the investigated materials, were acquired with a dedicated optical set up, composed of a quartz tungsten halogen lamp as the source of the white light, 300 mm focal length grating monochromator, and Si (for GeS) or InGaAs (for SnX) photodetector coupled with a lock-in amplifier (Stanford Research Systems SR830). The temperature of ≈80 K was achieved and maintained during the experiment with the use of a closed-cycle helium cryocooler and a heating system.

Ab initio calculations were performed within the framework of density functional theory (DFT) with the use of the relativistic projector-augmented waves (PAW) datasets[78] in Vienna Ab Initio Simulation Package (VASP).[79] The Perdew-Burke-Ernzerhof (PBE) parametrization of generalized gradients approximation (GGA) to the exchange-correlation functional was employed.[80] Monkhorst-Pack k-point grid of 12×12×3, plane wave energy cutoff of 600 eV, and a semi-empirical DFT-D3 correction for vdW interactions were used.[81] The electronic band structures were calculated with the use of two methods: Heyd-Scuseria-Ernzerhof (HSE06) hybrid functional,[82] and modified Becke-Johnson (mBJ-TB09) exchange potential.[83]

Supporting Information

Supporting Information is available from the Wiley Online Library or from the author.

Acknowledgements

This work was supported by the National Science Centre (NCN) Poland OPUS 15 no. 2018/29/B/ST7/02135. The publication was partially developed uder the provision of the Polish Ministry of Science and Higher Education project "Support for research and development with the use of infrastructure of the National Synchrotron Radiation Centre SOLARIS" under contract no. 1/SOL/2021/2. The authors acknowledge the SOLARIS Centre for the acces to the Beamline URANOS, where the measurements were performed. Computational studies were supported by the Wroclaw Centre for Networking and Supercomputing and the Interdisciplinary Centre for Mathematical and Computational Modelling, University of Warsaw. S.T. acknowledges NSF DMR-1955889, NSF CMMI-1933214, NSF 1904716, NSF 1935994, NSF ECCS 2052527, DMR 2111812, and CMMI 2129412.

Conflict of interest

The authors declare no conflict of interest.

Data Availability Statement

The data that support the findings of this study are available from the corresponding author upon reasonable request.

Keywords

ARPES, photoemission, thermoelectric materials, van der Waals crystals

Received: August 23, 2023
Published online: October 18, 2023

---

[1] L. C. Gomes, A. Carvalho, *Phys. Rev. B* **2015**, *92*, 085406.
[2] R. E. Banai, M. W. Horn, J. R. S. Brownson, *Sol. Energy Mater. Sol. Cells* **2016**, *150*, 112.
[3] K. Kushnir, M. Wang, P. D. Fitzgerald, K. J. Koski, L. V. Titova, *ACS Energy Lett.* **2017**, *2*, 1429.
[4] P. Zhao, H. Yang, J. Li, H. Jin, W. Wei, L. Yu, B. Huang, Y. Dai, *J. Mater. Chem. A* **2017**, *5*, 24145.
[5] S.-C. Liu, Y. Mi, D.-J. Xue, Y.-X. Chen, C. He, X. Liu, J.-S. Hu, L.-J. Wan, *Adv. Electron. Mater.* **2017**, *3*, 1700141.
[6] X. Zhou, X. Hu, B. Jin, J. Yu, K. Liu, H. Li, T. Zhai, *Adv. Sci.* **2018**, *5*, 1800478.
[7] X. Fan, L. Su, F. Zhang, D. Huang, D. K. Sang, Y. Chen, Y. Li, F. Liu, J. Li, H. Zhang, H. Xie, *ACS Appl. Mater. Interfaces* **2019**, *11*, 47197.
[8] L. C. Gomes, A. Carvalho, A. H. Castro Neto, *Phys. Rev. B* **2015**, *92*, 214103.
[9] R. Fei, W. Li, J. Li, L. Yang, *Appl. Phys. Lett.* **2015**, *107*, 173104.
[10] A. I. Lebedev, *J. Appl. Phys.* **2018**, *124*, 164302.
[11] G. Ding, G. Gao, K. Yao, *Sci. Rep.* **2015**, *5*, 9567.
[12] A. Shafique, Y.-H. Shin, *Sci. Rep.* **2017**, *7*, 506.
[13] R. Guo, X. Wang, Y. Kuang, B. Huang, *Phys. Rev. B* **2015**, *92*, 115202.
[14] K. Biswas, J. He, I. D. Blum, C.-I. Wu, T. P. Hogan, D. N. Seidman, V. P. Dravid, M. G. Kanatzidis, *Nature* **2012**, *489*, 414.
[15] M. Rakshit, D. Jana, D. Banerjee, *J. Mater. Chem. A* **2022**, *10*, 6872.
[16] B. Ul Haq, S. Alfaify, A. Laref, R. Ahmed, M. F. M. Taib, *Ceram. Int.* **2019**, *45*, 15122.
[17] Z. Wang, C. Fan, Z. Shen, C. Hua, Q. Hu, F. Sheng, Y. Lu, H. Fang, Z. Qiu, J. Lu, Z. Liu, W. Liu, Y. Huang, Z.-A. Xu, D. W. Shen, Y. Zheng, *Nat. Commun.* **2018**, *9*, 47.
[18] K. Zhang, K. Deng, J. Li, H. Zhang, W. Yao, J. Denlinger, Y. Wu, W. Duan, S. Zhou, *Phys. Rev.* **2018**, *2*, 054603.
[19] J. Cui, C. Chen, W. He, J. Avila, L.-D. Zhao, M. C. Asensio, J. He, Y. Chen, *J. Mater. Chem. A* **2018**, *6*, 24588.
[20] S. Li, J. Sun, Y. Zhang, Y. Fan, X. Tang, G. Tan, *Z. Anorg. Allg. Chem.* **2022**, *648*, e202200038.
[21] H. Tang, J.-F. Dong, F.-H. Sun, Asfandiyar, P. Shang, J.-F. Li, *Sci. China Mater.* **2019**, *62*, 1005.
[22] Y. Pei, X. Shi, A. Lalonde, H. Wang, L. Chen, G. J. Snyder, *Nature* **2011**, *473*, 66.
[23] J. Q. Li, N. Yang, S. M. Li, Y. Li, F. S. Liu, W. Q. Ao, *J. Electron. Mater.* **2018**, *47*, 205.
[24] K. Kuroki, R. Arita, *J. Phys. Soc. Jpn.* **2007**, *76*, 083707.
[25] L.-D. Zhao, G. Tan, S. Hao, J. He, Y. Pei, H. Chi, H. Wang, S. Gong, H. Xu, V. P. Dravid, C. Uher, G. J. Snyder, C. Wolverton, M. G. Kanatzidis, *Science* **2016**, *351*, 141.
[26] C. W. Wang, Y. Y. Y. Xia, Z. Tian, J. Jiang, B. H. Li, S. T. Cui, H. F. Yang, A. J. Liang, X. Y. Zhan, G. H. Hong, S. Liu, C. Chen, M. X. Wang, L. X. Yang, Z. Liu, Q. X. Mi, G. Li, J. M. Xue, Z. K. Liu, Y. L. Chen, *Phys. Rev. B* **2017**, *96*, 165118.
[27] I. Pletikosic, F. Von Rohr, P. Pervan, P. K. Das, I. Vobornik, R. J. Cava, T. Valla, *Phys. Rev. Lett.* **2018**, *120*, 156403.
[28] Q. Lu, M. Wu, D. Wu, C. Chang, Y.-P. Guo, C.-S. Zhou, W. Li, X.-M. Ma, G. Wang, L.-D. Zhao, L. Huang, C. Liu, J. He, *Phys. Rev. Lett.* **2017**, *119*, 116401.
[29] T. Nagayama, K. Terashima, T. Wakita, H. Fujiwara, T. Fukura, Y. Yano, K. Ono, H. Kumigashira, O. Ogiso, A. Yamashita, Y. Takano, H. Mori, H. Usui, M. Ochi, K. Kuroki, Y. Muraoka, T. Yokoya, *Jpn. J. Appl. Phys.* **2017**, *57*, 010301.
[30] K. Peng, B. Zhang, H. Wu, H. Che, X. Sun, J. Ying, G. Wang, Z. Sun, G. Wang, X. Zhou, X. Chen, *J. Mater. Chem. C* **2020**, *8*, 9345.
[31] M. Maeda, K. Yamamoto, T. Mizokawa, N. L. Saini, M. Arita, H. Namatame, M. Taniguchi, G. Tan, L. D. Zhao, M. G. Kanatzidis, *Phys. Rev. B* **2018**, *97*, 121110.
[32] L.-D. Zhao, S.-H. Lo, Y. Zhang, H. Sun, G. Tan, C. Uher, C. Wolverton, V. P. Dravid, M. G. Kanatzidis, *Nature* **2014**, *508*, 373.
[33] Y. Xiao, C. Chang, Y. Pei, D. Wu, K. Peng, X. Zhou, S. Gong, J. He, Y. Zhang, Z. Zeng, L.-D. Zhao, *Phys. Rev. B* **2016**, *94*, 125203.
[34] J. Carrete, N. Mingo, S. Curtarolo, *Appl. Phys. Lett.* **2014**, *105*, 101907.
[35] W. He, D. Wang, J.-F. Dong, Y. Qiu, L. Fu, Y. Feng, Y. Hao, G. Wang, J. Wang, C. Liu, J.-F. Li, J. He, L.-D. Zhao, *J. Mater. Chem. A* **2018**, *6*, 10048.
[36] Z. Tian, C. Guo, M. Zhao, R. Li, J. Xue, *ACS Nano* **2017**, *11*, 2219.
[37] I. Suzuki, S. Kawanishi, K. Tanaka, T. Omata, S.-I. Tanaka, *Electron. Struct.* **2022**, *4*, 025004.
[38] I. Suzuki, Z. Lin, S. Kawanishi, K. Tanaka, Y. Nose, T. Omata, S.-I. Tanaka, *Phys. Chem. Chem. Phys.* **2022**, *24*, 634.
[39] P. Mishra, H. Lohani, A. K. Kundu, R. Patel, G. K. Solanki, K. S. R. Menon, B. R. Sekhar, *Semicond. Sci. Technol.* **2015**, *30*, 075001.
[40] Z. Muhammad, Y. Li, G. Abbas, M. Usman, Z. Sun, Y. Zhang, Z. Lv, Y. Wang, W. Zhao, *Adv. Electron. Mater.* **2022**, *8*, 2101112.
[41] X. Zhang, J. Shen, S. Lin, J. Li, Z. Chen, W. Li, Y. Pei, *J. Materiomics* **2016**, *2*, 331.
[42] L. Shaabani, S. Aminorroaya-Yamini, J. Byrnes, A. Akbar Nezhad, G. R. Blake, *ACS Omega* **2017**, *2*, 9192.
[43] W. Li, C. Yang, *AIP Adv.* **2022**, *12*, 085111.
[44] Y. Wang, X. Yang, Y. Shang, *Phys. Lett. A* **2019**, *383*, 2499.
[45] W. Li, C. Yang, *J. Appl. Phys.* **2022**, *132*, 214302.
[46] M. Rakshit, S. Nath, S. Chowdhury, R. Mondal, D. Banerjee, D. Jana, *Phys. Scr.* **2022**, *97*, 125804.
[47] A. Rahim, W. Haider, A. Khan, H. Khan, H. U. Din, M. Shafiq, B. Amin, M. Idrees, *J Comput Electron* **2022**, *21*, 725.
[48] A. Marjaoui, M. Ait Tamerd, M. Zanouni, A. El Kasmi, M. Assebban, M. Diani, *Mater. Sci. Eng., B* **2022**, *281*, 115737.

[49] Z. Bian, H. Wang, Q. Zhou, A. Shakouri, *Phys. Rev. B* **2007**, *75*, 245208.
[50] D. Tan, H. E. Lim, F. Wang, N. B. Mohamed, S. Mouri, W. Zhang, Y. Miyauchi, M. Ohfuchi, K. Matsuda, *Nano Res.* **2017**, *10*, 546.
[51] J. Liu, S. T. Pantelides, *Appl. Phys. Express* **2018**, *11*, 101301.
[52] A. Tolloczko, S. J. Zelewski, M. Blaszczak, T. Wozniak, A. Siudzinska, A. Bachmatiuk, P. Scharoch, R. Kudrawiec, *J. Mater. Chem. C* **2021**, *9*, 14838.
[53] V. L. Le, D. D. Cuong, H. T. Nguyen, X. A. Nguyen, B. Kim, K. Kim, W. Lee, S. C. Hong, T. J. Kim, Y. D. Kim, *AIP Adv.* **2020**, *10*, 105003.
[54] R. Oliva, T. Wozniak, F. Dybala, A. Tolloczko, J. Kopaczek, P. Scharoch, R. Kudrawiec, *Phys. Rev. B* **2020**, *101*, 235205.
[55] Y. Cui, Z. Zhou, X. Wang, X. Wang, Z. Ren, L. Pan, J. Yang, *Nano Res.* **2021**, *14*, 2224.
[56] Z. Chen, W. Hwang, M. Cho, A. T. Hoang, M. Kim, D. Kim, D. H. Kim, Y. D. Kim, H. J. Kim, J.-H. Ahn, A. Soon, H.-J. Choi, *NPG Asia Mater* **2022**, *14*, 41.
[57] C.-H. Ho, W.-Y. Lin, L.-C. Chao, K.-Y. Lee, J. Inagaki, H.-C. Hsueh, *ACS Appl. Energy Mater.* **2020**, *3*, 4896.
[58] H. Wang, X. Qian, *2D Mater.* **2017**, *4*, 015042.
[59] R. Fei, W. Kang, L. Yang, *Phys. Rev. Lett.* **2016**, *117*, 097601.
[60] M. Wu, X. C. Zeng, *Nano Lett.* **2016**, *16*, 3236.
[61] Y. I. Jhon, J. Lee, M. Seo, J. H. Lee, Y. M. Jhon, *Adv. Opt. Mater.* **2019**, *7*, 1801745.
[62] H. R. Yang, X. M. Liu, *Appl. Phys. Lett.* **2017**, *110*, 171106.
[63] A. Dasgupta, J. Gao, X. Yang, *Laser Photonics Rev.* **2020**, *14*, 1900416.
[64] M. Zhu, M. Zhong, X. Guo, Y. Wang, Z. Chen, H. Huang, J. He, C. Su, K. P. Loh, *Adv. Opt. Mater.* **2021**, *9*, 2101200.
[65] P. A. E. Murgatroyd, M. J. Smiles, C. N. Savory, T. P. Shalvey, J. E. N. Swallow, N. Fleck, C. M. Robertson, F. Jäckel, J. Alaria, J. D. Major, D. O. Scanlon, T. D. Veal, *Chem. Mater.* **2020**, *32*, 3245.
[66] J. D. Wiley, W. J. Buckel, R. L. Schmidt, *Phys. Rev. B* **1976**, *13*, 2489.
[67] H. R. Chandrasekhar, R. G. Humphreys, U. Zwick, M. Cardona, *Phys. Rev. B* **1977**, *15*, 2177.
[68] T. J. Whittles, L. A. Burton, J. M. Skelton, A. Walsh, T. D. Veal, V. R. Dhanak, *Chem. Mater.* **2016**, *28*, 3718.
[69] M. J. Smiles, J. M. Skelton, H. Shiel, L. A. H. Jones, J. E. N. Swallow, H. J. Edwards, P. A. E. Murgatroyd, T. J. Featherstone, P. K. Thakur, T.-L. Lee, V. R. Dhanak, T. D. Veal, *J. Mater. Chem. A* **2021**, *9*, 22440.
[70] P. Sutter, S. Wimer, E. Sutter, *Nature* **2019**, *570*, 354.
[71] N. Zawadzka, L. Kipczak, T. Wozniak, K. Olkowska-Pucko, M. Grzeszczyk, A. Babinski, M. R. Molas, *Nanomaterials* **2021**, *11*, 3109.
[72] V. Tayari, B. V. Senkovskiy, D. Rybkovskiy, N. Ehlen, A. Fedorov, C.-Y. Chen, J. Avila, M. Asensio, A. Perucchi, P. Di Pietro, L. Yashina, I. Fakih, N. Hemsworth, M. Petrescu, G. Gervais, A. Grüneis, T. Szkopek, *Phys. Rev. B* **2018**, *97*, 045424.
[73] P. Wu, B. Zhang, K. L. Peng, M. Hagihala, Y. Ishikawa, M. Kofu, S. H. Lee, H. Kumigashira, C. S. Hu, Z. M. Qi, K. Nakajima, G. Y. Wang, Z. Sun, T. Kamiyama, *Phys. Rev. B* **2018**, *98*, 094305.
[74] A. Khandelwal, K. Mani, M. H. Karigerasi, I. Lahiri, *Mater. Sci. Eng., B* **2017**, *221*, 17.
[75] J. Tauc, *Mater. Res. Bull.* **1968**, *3*, 37.
[76] Y. Zhong, L. Zhang, W. Chen, H. Zhu, *Nanotechnology* **2020**, *31*, 385203.
[77] J. Szlachetko, J. Szade, E. Beyer, W. Blachucki, P. Ciochon, P. Dumas, K. Freindl, G. Gazdowicz, S. Glatt, K. Gula, J. Hormes, P. Indyka, A. Klonecka, J. Kolodziej, T. Kolodziej, J. Korecki, P. Korecki, F. Kosiorowski, K. Kosowska, G. Kowalski, M. Kozak, P. Koziol, W. Kwiatek, D. Liberda, H. Lichtenberg, E. Madej, A. Mandziak, A. Marendziak, K. Matlak, A. Maximenko, et al., *Eur Phys J Plus* **2023**, *138*, 10.
[78] G. Kresse, D. Joubert, *Phys. Rev. B* **1999**, *59*, 1758.
[79] G. Kresse, J. Furthmüller, *Phys. Rev. B* **1996**, *54*, 11169.
[80] J. P. Perdew, K. Burke, M. Ernzerhof, *Phys. Rev. Lett.* **1996**, *77*, 3865.
[81] S. Grimme, J. Antony, S. Ehrlich, H. Krieg, *J. Chem. Phys.* **2010**, *132*, 154104.
[82] A. V. Krukau, O. A. Vydrov, A. F. Izmaylov, G. E. Scuseria, *J. Chem. Phys.* **2006**, *125*, 224106.
[83] F. Tran, P. Blaha, *Phys. Rev. Lett.* **2009**, *102*, 226401.